On the scales of dynamic topography in whole-mantle convection models

M. Arnould[a,b,c,*], N. Coltice[a], N. Flament[c], V. Seigneur[d], R.D. Müller[b]

[a] *Laboratoire de Géologie de Lyon, Terre, Planètes, Environnement, CNRS UMR 5276, Université de Lyon, École Normale Supérieure de Lyon, Université Claude Bernard, 2 rue Raphaël Dubois, Villeurbanne 69622, France*
[b] *EarthByte Group, School of Geosciences, Madsen Building F09, University of Sydney, NSW 2006, Australia*
[c] *School of Earth and Environmental Sciences, University of Wollongong, Northfields Avenue, Wollongong, NSW 2522, Australia*
[d] *Unité de Mathématiques Pures et Appliquées, CNRS UMR 5669, Université de Lyon, École Normale Supérieure de Lyon, 46 Allée d'Italie, 69364 Lyon Cedex 07, France*

Abstract

Mantle convection contributes to shaping Earth's surface by generating dynamic topography. Recent observational constraints on present-day residual topography suggest that surface topography is sensitive to mantle flow down to $\sim$ 1,000 km scale. At this scale, surface processes such as erosion, sedimentation and relative sea-level change, have shorter response times. However, time-dependent global mantle flow models do not produce these scales of dynamic topography yet.

Here, we present numerical models of mantle convection in 2D-spherical annulus geometry at high Rayleigh number, with large radial and lateral viscosity contrasts. We first identify the parameter space in which models self-generate plate-like behaviour, surface heat flow, surface velocities and total

*Corresponding author.
Email address: maelis.arnould@ens-lyon.fr (M. Arnould)

topography that are comparable with Earth's. These models produce both whole mantle convection and smaller-scale upper-mantle convection, which in turn results in small- (< 500 km) to large-scale ($> 10,000$ km) dynamic topography. We show the importance of taking into account large viscosity contrasts in order to generate a large range of space and time scales of dynamic topography. We investigate the time-dependence of dynamic topography across scales, in the light of the history of the tectonic and convective processes from which they originate.

Keywords: Dynamic topography, mantle convection, small-scale convection, subduction, LLSVP

1. Introduction

Surface elevation results from both external and internal processes that continuously shape the Earth over a wide range of rhythms and scales. Mantle flow, by transporting temperature and density anomalies and deforming the surface, generates dynamic topography, a mechanism first proposed by Pekeris (1935).

Global models of mantle flow and density have generated predictions of Earth's dynamic topography. Despite the different methods used, these studies attribute large-scale topography anomalies (wavelengths longer than 10^4 km) to whole mantle convection (Hager and Richards (1989); Ricard et al. (1993)). For example, Lithgow-Bertelloni and Silver (1998) invoked large-scale whole-mantle upwelling flow to explain large topography anomalies such as the African superswell, and Mitrovica et al. (1989) showed that slabs sinking into the mantle could explain the evolution of intra-continental sedimentary basins such as the Western Interior Seaway in North America.

However, observational constraints of transient ($\sim$ 1 Myr) and localised ($<$ 3,000 km) vertical motions of Earth's surface (Hartley et al., 2011), and models of dynamic topography and relative sea level change associated with small-scale convection (Petersen et al., 2010) confirm that dynamic topography should be particularly sensitive to shallow density heterogeneities at short to intermediate wavelengths (Hager and Richards, 1989). A recent global model of present-day residual topography derived from seismic data collected worldwide, mainly at passive margins (Hoggard et al., 2016), also suggests that the amplitude of residual topography is significant down to $\sim$ 1,000 km scale. Global mantle convection models do not predict these smaller scales of topography, presumably because these models lack small to intermediate-scale convective motions, especially in the uppermost mantle. The computational limitation in the global convection models is to account for the extreme lateral viscosity variations caused by temperature and stress-dependencies. Since large radial and lateral viscosity contrasts produce short wavelengths of mantle convection (Moresi and Solomatov, 1995; Solomatov and Moresi, 2000; Coltice et al., 2017a), we propose to compute dynamic topography in 2D-spherical annulus numerical models of mantle convection (Hernlund and Tackley, 2008) for which large viscosity contrasts are computationally tractable.

The models we present account for large convective vigour, the presence of continents and deep-seated thermo-chemical piles in order to link temporal and spatial scales of predicted dynamic topography. We first identify a range of models according to the following criteria: self-generation of plate-like behaviour (Tackley, 2000), surface heat flow, surface velocities and topography distribution comparable to Earth's. In the selected models, the predicted dynamic topography, which we compute by removing the model isostatic topography from the total model topography, includes both small scales (< 500 km) and large scales ($> 10^4$ km). This allows us to investigate the role of small-scale convection, slabs, plumes and deep-seated thermo-chemical heterogeneities in controlling the patterns and timescales of dynamic topography evolution.

2. Methods

2.1. Two-dimensional convection models with self-consistent plate generation

2.1.1. Equations

We solve the following non-dimensionalised equations (1) of mass, momentum, energy and composition conservation in 2D-spherical annulus geometry, under the Boussinesq approximation of an incompressible mantle (*e.g.* Ricard, 2015):

$$\begin{aligned} \nabla \cdot \mathbf{v} &= 0 \\ \nabla p - \nabla \cdot \left[\eta(\underline{\nabla \mathbf{v}} + (\underline{\nabla \mathbf{v}})^T)\right] &= Ra(\alpha(z)T + BC)\mathbf{e_r} \\ \frac{DT}{Dt} &= -\nabla \cdot (\nabla T) + H \\ \frac{DC}{Dt} &= 0 \end{aligned} \tag{1}$$

where $\mathbf{v}$ is the velocity vector, p the dynamic pressure, η the viscosity, T the temperature, C the composition (to represent continents and deep thermo-chemical piles), Ra the Rayleigh number based on the temperature drop across the mantle and thermal expansivity at room pressure, $\alpha(z)$ is the depth-dependent thermal expansivity, H the heat production rate, B the chemical buoyancy ratio and $\mathbf{e_r}$ is the radial unit vector. $D/Dt = \partial/\partial t + (\mathbf{v} \cdot \nabla)$ indicates the Lagrangian time derivative.

We use a depth-dependent thermal expansivity law obtained from Raman mode frequency shifts of Mg-SiO3-perovskite in diamond-anvil-cell experiments and extrapolated to lower-mantle pressure and temperature range (Gillet et al., 2000). Decreasing the thermal expansivity by a factor of 5 with pressure (Chopelas and Boehler, 1992) broadens thermal anomalies in the deep mantle, stabilises thermo-chemical heterogeneities (Hansen et al., 1993), and favours slab stagnation and hotter mantle plumes (Tosi et al., 2013).

Viscosity depends exponentially on pressure and temperature as follows:

$$\eta(z,T) = \eta_0 \times exp\Big(A + \frac{E_a + PV_a}{RT}\Big) \quad (2)$$

where η_0 is the reference non-dimensionalised viscosity value, A is chosen so that $\eta = \eta_0$ for $T = 0.64$ (the *a priori* temperature at the base of the lithosphere), E_a is the activation energy , P is the static pressure, V_a is the activation volume, R is the gas constant and T is the temperature. We consider a viscosity jump by a factor of 30 at the upper-lower mantle boundary, as suggested by geoid and postglacial rebound studies (Nakiboglu and Lambeck (1980); Ricard et al. (1993)). For computationnal reasons, we apply a maximum viscosity cutoff to limit the resulting viscosity variations to 6 orders of magnitude throughout the mantle domain (Fig. 1), consistently with the study of King (2009) showing that such a high value of the cut-off would produce topography errors $< 5\%$.

We use a pseudo-plastic rheological law enabling strain localisation (Tackley, 2000) based on the following yield stress threshold:

$$\sigma_Y = \sigma_Y + z \times d\sigma_Y \tag{3}$$

where the yield stress at the surface σ_Y has different values for different materials, and $d\sigma_Y$ is the yield stress depth derivative. When the yield stress σ_Y is reached, the viscosity η_Y drops markedly following:

$$\eta_Y = \frac{\sigma_Y}{2\dot{\epsilon}_{\mathrm{II}}} \tag{4}$$

where $\dot{\epsilon}_{\mathrm{II}} = \sqrt{0.5\dot{\epsilon}_{ij}\dot{\epsilon}_{ij}}$, the second invariant of the strain rate tensor. This enables the localisation of deformation (4) in order to mimic dynamics of plate boundaries (*e.g.* Tackley, 2000) and seafloor area-age distribution (Coltice et al., 2012) at Earth's surface.

The range of parameters we explored is in Table 1 and Supplementary Table SI 1.

2.1.2. Set up

We computed a series of models (Fig. 1) with the convection code StagYY (Tackley, 2000). The 2D-spherical annulus geometry makes it possible to compute mantle flow models that are comparable to 3D spherical models without being computationally as expensive (Hernlund and Tackley, 2008). Free-slip conditions are used at both the core-mantle boundary and the surface. The lateral resolution is about 25 km at the surface and the radial resolution varies between 26 km and 13 km due to a mesh refinement at boundaries.

We use 1.6×10^7 tracers and the tracer-ratio method (Tackley and King, 2003) to evaluate compositional fields. We set the initial thickness and excess density of the thermo-chemical layer (when considered) in order to obtain stable thermo-chemical piles through time following geodynamical experimental (Davaille et al., 2003) and numerical (Deschamps and Tackley, 2009) studies. Although the thermal or thermo-chemical nature of Large-Low Shear Velocity Provinces (LLSVPs) is still debated (Garnero et al., 2016), we choose a maximum height of about 1,000 km above the core-mantle boundary for the volume of the basal layer. We consider two continental lithospheric rafts that are stiffer than oceanic lithosphere to remain stable throughout the time of integration (Lenardic and Moresi, 1999). They cover 30% of the surface area and are divided into 3 parts (Fig. 1): cratons at the center, surrounded by proterozoic belts and mobile belts, in order of decreasing viscosity and density (see Table 1). We first obtain an initial condition from the last step of a long equilibration phase in which all tracers are fixed (continents do not move and the thermo-chemical heterogeneity is a uniform layer). The initial condition is in statistical steady-state for average mantle temperature and basal and surface heat flux. From such initial conditions, we compute a thermo-chemical evolution with moving tracers over $\sim$1000 Myr, in order to compute statistics and observe a diversity of convective states. Each of these models is computationally expensive, because of the long time of integration, high resolution and solving for extreme viscosity variations.

We compute a series of models to find a parameter range for which (1) we obtain plate-like behaviour and (2) we predict amplitudes of topography and surface heat flow comparable to observations (see Fig. 2 and Supplementary Table SI 1). We vary Ra between 10^5 and 5×10^7. Basal heating represents on average 6 to 25% of the total surface heat flux (Supplementary Table SI 1). We also vary the dimensional value of the yield stress at room pressure between 1 and 130 MPa (Fig. 2). These values are low compared to laboratory experiments on mantle rocks (Brace and Kohlstedt, 1980), and close to the stress drop of earthquakes (Allmann and Shearer, 2009). The pseudo-plastic rheology used here is empirical, and probably represents homogenisation of a variety of processes (such as two-phase flow, grain size evolution, damage, etc...) that occur at smaller spatial scales than resolved in our models. In practice, larger yield stresses in our models systematically result in the formation of a stagnant lid at the surface of the domain (Fig. 2).

We first determine models in plate-like behaviour using the same diagnostics as Tackley (2000). We measure the plateness P here expressed as

$$P = 1 - \frac{f_{90}}{0.6},$$

where f_{90} corresponds roughly to the proportion of the surface localising 90 % of deformation, and the value of 0.6 is f_{90} for a model with a constant viscosity. This proportion is about 0.6 for models with $Ra \geq 10^6$ and 0.54 for models with $Ra = 10^5$. A perfect plateness is 1. We also measure the mobility that is the ratio of the RMS surface velocity to RMS velocity in the whole domain. Plate-like behaviour requires mobility close to or larger than 1. Among the models passing this test, we keep those which display heat flow and total topography close to Earth's (see Fig. 2 and Supplementary Table SI 1). We verify that the surface topography distribution is bimodal and comparable to Earth's topography (see Supplementary Fig. SI 2). We obtain six models that pass both tests. However, the RMS topography in these selected models is still 500 m to 1 km larger than Earth's air-loaded topography. This could be because the density difference between continental and oceanic lithosphere is overestimated in the models, as shown by the differences between our models' hypsometric curve and Earth's on Supplementary Fig. SI 2.

We choose to focus on five models. Model 9 ($\sigma_Y = 18$ MPa), Model 10 ($\sigma_Y = 27$ MPa) and Model 13 ($\sigma_Y = 48$ MPa) have a chemical basal layer and $Ra = 10^7$. Model 11 ($\sigma_Y = 28$ MPa) has no chemical basal layer and $Ra = 10^7$. Finally, Model 18 ($\sigma_Y = 25$ MPa) has a chemical basal layer and $Ra = 5 \times 10^7$ (Supplementary Table SI 1). The time-averaged power spectra of temperature heterogeneities in these five models display strong low degrees, and a contribution from smaller scales in the shallow mantle (Fig. 1a and 3), similarly to seismic tomographic models like S40RTS (Ritsema et al., 2011). Degree 1 is dominant in the lower mantle for the spectra of Models 9,10 and 13. In Model 11, the spectrum in the lower mantle is dominated by degree 2. The presence of deep-seated thermo-chemical heterogeneities enhances the power of degrees lower than 4. Increasing Ra breaks the degree 1 symmetry of the basal thermo-chemical layer and leads to strong degrees up to 7 in the lowermost mantle.

2.2. Computing dynamic topography

Many studies compute dynamic topography as a result from the normal stresses arising from the convecting mantle, and exclude the density anomalies located above a depth of 220 to 350 km, since the non-convecting lithosphere extends down to these depths in some places (Steinberger, 2007;

Lithgow-Bertelloni and Silver, 1998; Flament et al., 2013). Contrarily to these models, the numerical solutions we present here express shallow smaller-scale convection near the lithosphere-asthenosphere boundary. Therefore, using the same method would remove a potential strong component of dynamic topography. We thus compute dynamic topography in a similar fashion to present-day residual topography (*e.g.* Gvirtzman et al., 2016). We consider dynamic topography as the vertical motion of the surface induced by mantle flow below the lithosphere (which is the upper conductive thermal boundary layer), in contrast to isostatic topography occurring above the lithosphere-asthenosphere boundary. We first calculate total topography from normal stresses at the surface σ_{zz} as follows:

$$h = \frac{\sigma_{zz}}{\rho g} \tag{5}$$

where ρ is the non-dimensional density and g is the gravitational acceleration. We calculate isostatic topography as the sum of all density contributions above a compensation depth, following the Airy condition (Fig. 4a), and normalise it by subtracting the average value in order to account for the conservation of the average radius of our models. The compensation depth is taken as the inflection point of the average geotherm of the model (which is influenced by the thermal state of continents) at each timestep, and varies between 240 and 360 km depth depending on the temperature field. This method ensures that the modelled isostatic topography contains the density variations of both continental and oceanic lithospheres. Setting an arbitrary constant compensation depth ranging between 250 km and 350 km does not affect the spatial patterns of dynamic topography but shifts the values of dynamic topography by about 100 m in average. We assume that the topography at subduction zones is completely dynamic since the Airy condition of pressure balance at the compensation depth cannot be satisfied there. We detect subduction zones from their large negative normal velocity. The lateral influence of subduction zones on dynamic topography lows at trenches varies from 200 km to 500 km in lateral extent depending on dip angles. We conservatively set isostatic topography to zero within 500 km of subduction zones. This approach ensures that subduction topography is dynamic although the lateral extent of steeply dipping subduction zones is overestimated. Setting the isostatic topography to zero within a shorter or larger lateral distance of subduction zones does not change our conclusions about the global spatial distribution of dynamic topography (see Supplementary Fig. SI 4). We obtain the dynamic component of topography by subtracting the isostatic topography from total topography.

On Fig. 4b, we decompose total topography (blue curve) into its isostatic (red curve) and dynamic (yellow curve) components for a snapshot of Model 10. The isostatic topography follows the shape of total topography, emphasising its dominant role in the generation of topography (Gvirtzman et al., 2016). The amplitude of dynamic topography is ± 2 km at most, except at subduction zones that we have considered to be entirely dynamic. The long-wavelength trend of dynamic topography (> 5000 km) is consistent with the longest wavelength of mantle convection, outlined by the location of large-scale density anomalies in the model at this timestep (Fig. 4a).

Short-wavelength variation in dynamic topography ($\sim$ 200-500 km) is present under continents and under old oceanic lithosphere (Fig. 4b). It results from small-scale convection below the lithosphere (Fig. 1). Small-scale dynamic topography is also caused by small-scale convection at continental boundaries (also called edge-driven convection) and by artificial excessive stresses at the boundaries between the different continental belts. These artifacts do not affect our conclusions, as we do not focus on processes affecting continental margins. The description of this snapshot confirms that the predicted dynamic topography is directly linked to density anomalies advected within the mantle, as expected.

3. Results

3.1. Spatial distribution of dynamic topography

Fig. 5 shows the evolution of total topography and its components through time for Model 10. Here, the two continents move freely and never collide. Continental total topography decreases through time by about 1 km due to the combination of two phenomena. First, the presence of an initial hot area below continents, favoured by their fixity during the equilibration phase and their insulating effect (see Gurnis, 1993) provides sub-continental positive buoyancy that slowly decreases as continents start moving. Continents present an average sligthly positive (78 m in average) dynamic topography throughout the period of interest due to this insulation characteristic (Fig. 5c). Second, the progressive thermal erosion of continental lithosphere throughout the model evolution contributes to the lowering of their height through time, as seen in the concomitant decrease of isostatic topography on Fig. 5b. This is a model effect that may not apply to Earth. Continents also get deflected downwards at convergent margins. Subduction zones generally initiate within 3000 km of a continental margin in this model. Depending on the geometry of slabs sinking in the mantle, dynamic topography around subduction zones is asymmetric, being more negative directly above the dense sinking material. Small-scale dynamic topography develops below old oceanic lithosphere and continents, as expected for Earth (Haxby and Weissel (1986)).

Models 9, 11, 13 and 18 present similar characteristics to Model 10 for total, isostatic and dynamic topography (Supplementary Fig. SI 3). However, in Model 9, 11 and 13, continents collide and form a supercontinent during the second half of the time integration. The number of subduction zones decreases as the yield stress increases, favouring the development of old oceanic lithosphere subjected to small-scale convection and dynamic topography in Model 13. The amplitude of dynamic topography is also smaller for Model 13. In Model 11, dynamic topography highs are higher than in Model 10 because heat evacuation is more efficient in the absence of thermo-chemical deep piles. Indeed, in Model 10, the presence of denser material at the base of the mantle opposes the positive buoyancy of ascending plumes and limits their vertical velocity. Therefore, in Model 11, plumes are more positively buoyant and deflect the surface more than in Model 10. In the absence of dense basal structures, the distribution of subduction zones is more homogeneous than in Model 10. The location of subduction initiation is independent from their distance to a continental margin. In Model 18, the larger convective vigour leads to smaller convective scales than in Model 10 although it has the same dimensional yield stress. The amplitude of dynamic topography in Model 18 is intermediate between that of Model 9 and that of

Model 10.

3.2. *Spectral decomposition of dynamic topography*

We compute the spatial Fourier power spectrum of the average dynamic topography for all five models in order to characterize the spatial power distribution of dynamic topography. To compare these Fourier power spectra with existing spherical harmonics power spectra of global dynamic topography (*e.g.* Flament et al., 2013) and residual topography (Hoggard et al., 2016), we calculate and normalise the Fourier spectrum of our models thanks to the method described in Supplementary section SI 1.

The power spectrum of dynamic topography in our models (Fig. 6) is characterised by a large power at low degrees (> 1 km^2, for degrees 1 to 4) and a substantial power ($> 2 \times 10^{-2}$ km^2) for intermediate scales of dynamic topography (degree 4-30). The presence of deep thermo-chemical piles results in a lower amplitude of the largest wavelengths of dynamic topography, but not the intermediate to small wavelengths. This is because positive thermal buoyancy is offset by negative chemical buoyancy. The overall shape of the power spectrum does not depend on the dense basal structures, despite differences in the planform of convection as seen on Fig. 3.

Increasing the yield stress decreases the power at all spherical harmonic degrees. Indeed, if we compare the thermal heterogeneity spectra of models 9, 10 and 13 (Fig. 3), we see that the increase of the yield stress leads to decrease of the power of intermediate wavelengths (spherical harmonic degrees 4-16), particularly in the upper mantle since less subduction zones develop and the interior of the mantle heats up, prohibiting the rise of mantle plumes. Therefore, a larger part of topography is isostatic for a higher yield stress.

In order to identify the sources of the different spectral signatures of dynamic topography, we use an order-5 Butterworth filter (Butterworth, 1930) to decompose the dynamic topography component of Model 10 (Fig. 5c) into large ($>$ 5000 km - spherical harmonic degree $l < 4$), intermediate (between 5000 km and 500 km - $4 < l < 80$) and small ($<$ 500 km - $l > 80$) scales (Fig. 7). This filter has a flat response in the passband and a continuous slope decrease to the stopband frequency (no ripples), avoiding the addition of noise to the filtered signal.

Large-scale dynamic topography highs (Fig. 7a) have a maximum amplitude of 1.4 km. Figure 8 shows that dynamic topography highs are correlated with the position of large-scale upwellings, themselves linked with the position of dense basal structures in Model 10. Large-scale dynamic topography lows (-2.1 km most) occur at subduction zones, which generally initiate on the sides of dense basal structures before moving towards continental edges. Dynamic topography highs are correlated with the position of continents before the formation of the supercontinent, but not after.

Filtering dynamic topography for intermediate scales (Fig. 7b) shows that the main process controlling dynamic topography at these spatial scales is subduction. Dynamic topography at subduction zones is generally asymmetric, the surface being deflected within 5000 km of lateral extent above the position of dense slabs. However, dynamic topography is symmetric above double-sided model subduction zones that are vertical throughout the upper mantle. Slabs generally stagnate at the transition zone, which leads to changes in their dip angle. This is reflected in the temporal changes of the spatial distribution of dynamic topography amplitudes on either of their sides. Continents are also affected by intermediate- to large-scale dynamic topography highs when plumes reach their base and propagate laterally.

Finally, all models show the existence of small-scale dynamic topography (Fig. 7c), particularly developed near subduction zones below oceanic lithosphere, with an amplitude of $\pm$ 750 m at most and a wavelength of $\sim$200 km. This results from the development of small-scale convection in the upper mantle. Small-scale convection also occurs below continental lithosphere producing dynamic topography wavelength of about 500 km. This is larger scale than for the oceanic lithosphere, because continents are ten to a thousand times more viscous. Small-scale dynamic topography also occurs at subduction zones. It is characterized by two positive dynamic topography anomalies surrounding a depression directly above the trench.

3.3. Temporal evolution of dynamic topography

Large-scale mantle convection drives the temporal evolution of large scale dynamic topography as highlighted by the superposition of the location of deep thermo-chemical heterogeneities, when present, and large-scale dynamic topography highs (Fig. 8).

Intermediate scales of dynamic topography are also subjected to variations through time, in connection with the number of subduction zones. As shown on Figure 9, the spectral power of intermediate spherical harmonic degrees experiences variations of about one order of magnitude. The decrease in the power of intermediate scales is associated with a decrease in the number of subduction zones. In Model 11, a similar decrease in the power of intermediate scales of dynamic topography appears just before continental collision, when the number of subduction zones decreases. In contrast, the initiation of subduction zones favours the development of intermediate wavelengths of dynamic topography. Variations in the number of subduction zones occur over 50 to 200 Myr in our models (Fig. 9). Changes in the dip angle of subduction zones also regionally modify the dynamic topography field around subduction zones on timescales of several tens of million years (Fig. 5 and 7b).

In all considered models, small-scale dynamic topography is linked to small-scale convection and subduction zones. Small-scale convection develops below moving plates and thus undergoes shearing deformation which deflects the moving cells (Fig. 1a). Short-lived cold droplets develop from the base of the lithosphere on timescales of the order of 1-10 Myr, thus deflecting the surface at this rhythm (Fig. 7c). Nevertheless, once a small-scale convective cell is formed, subsequent droplets initiate at the same location, which leads to longer lived dynamic topography oscillations (timescale of the order of $\sim$50-100 Myr) that only disappear when absorbed by a subduction zone. Local disturbances in the planform of small-scale convection are caused by the interplay between small-scale convection and rising plumes beneath oceanic lithosphere, which 'rejuvenate' its base and temporarily erase small-scale convection in the direct vicinity of the plume conduit.

4. Discussion

4.1. Model limitations

Despite the 2D-spherical annulus geometry being more accurate than the 2D-cartesian domain to represent the actual flow within the mantle (Hernlund and Tackley, 2008), temperature and density anomalies are still confined to a plane. Flow cannot propagate orthogonally to the 2D plane and thus generates dynamic topography wavelengths longer than expected since the rising material can only spread in one dimension below the lithosphere. The amplitudes of dynamic topography given in our models are thus an upper bound for the amplitudes generated in a corresponding 3D spherical model. Moreover, our spectral decomposition of dynamic topography assumes that the statistical distribution of dynamic topography is homogeneous in all directions on a complete sphere. However, the transposition of this generation of numerical models with an Earth-like Rayleigh number and large radial and lateral viscosity variations into time-dependent 3D spherical models is still computationally unreachable.

Even though the Rayleigh number, total heat flow and surface plate velocities of our models approach Earth-like values, these models do not fully capture the convective and plate behaviour of Earth since we made assumptions and simplifications to solve the problem of time-dependent convection. We do not consider mantle compressibility, which would affect the planform of convection, for computational reasons and not to add further complexity.

Our models employ a simplified rheology (for a review, see Coltice et al., 2017b), especially at low temperature where a diversity of deformation mechanisms coexist. For instance, we do not model the elasticity of lithosphere, which would at least partially filter out the shortest wavelengths of dynamic topography (Golle et al., 2012). Considering the elastic properties of the lithosphere would modify the behaviour of the highest-frequency surface deflections, depending on the modelled elastic thickness.

We used a free-slip condition at the surface. We thus derived dynamic topography from normal stresses acting on the top boundary, which can produce some artifacts, for example between continental belts or near subduction trenches. Even if the small-scale dynamic topography highs that appear on both sides of subduction zones in our models have been described as viscous bulges (Husson et al., 2012), Crameri et al. (2012a) showed that the use of a free surface precludes the formation of excessive normal stresses and results in a better resolution of topography. Crameri et al. (2012b) also demonstrated that single-sided subduction zones can be obtained by using a ‘sticky-air’ layer. Crameri et al. (2017) further compared the topography generated in models using a ’sticky-air layer’ with models using a free-slip surface boundary condition, and showed that the latter produces anomalous small-scale (500 km) dynamic topography in the direct vicinity of subduction zones due to the fixed surface. They showed that the use of a ’sticky-air’ layer limits artificial surface vertical deformations. Using a ‘sticky-air’ layer would thus better resolve the effect of small-scale convection (200-500 km) on dynamic topography. However, this approach drastically increases the computation cost because of the very low viscosity of the air layer. Moreover, since our surface topography amplitudes are small compared to the domain depth, using the free-slip simplification is still reasonable (Crameri et al., 2012a).

4.2. Spatial and temporal influence of dynamic topography on surface processes

The generation of multiple scales of dynamic topography induced by large viscosity contrasts reported herein provides a first step to the modelling of the interplay between the different scales of dynamic topography in global numerical models of mantle convection and on their multiple effects on surface processes. In the models presented, rapid flow reorganisations occur due to subduction initiation or slab breakoffs, changes in slab dip angles, small-scale convection dynamics and interaction between plume heads and the lithosphere. These processes produce dynamic topography over a range of spatial scales that cannot yet be taken into account in 3D global models because of computational limitations. Our models predict significant intermediate to small scales of dynamic topography, which correspond to the global residual topography of Hoggard et al. (2016) at spherical harmonic degrees larger than 5 (Fig. 6). A recent inversion (Yang and Gurnis, 2016) of present-day mantle structures to simultaneously fit the long-wavelength geoid, free-air gravity anomalies, gravity gradients and residual topography point data (Hoggard et al., 2016) results in a dynamic topography spectrum close to those we obtain. Lateral viscosity variations are also a key ingredient of the instantaneous model of Yang and Gurnis (2016). Nevertheless, we note a significant discrepancy at low spherical harmonic degrees (1-4) between global model dynamic topography spectra, including ours, and the residual topography spectrum of Hoggard et al. (2016), for which power is 10 times lower (Fig. 6). This discrepancy is extensively debated (*e.g.* Molnar et al., 2015; Hoggard et al., 2016; Yang and Gurnis, 2016; Hoggard et al., 2017), and our models do not have the power to resolve it.

At long to intermediate wavelengths, subduction dynamics control continental sedimentation by favouring regional continental flooding (Mitrovica et al., 1989). In our models, the bending of continents due to the presence of sinking slabs in the upper mantle can reach 5000 km in lateral extent (depending on slab geometry), up to 1.5 km amplitude and can last up to 50 Myr (Fig. 5c-f). The greatest deflections occur when subduction straddles a continental edge. In the case of the tectonic motion of continents over slabs, we observe a propagation of topographic lows towards the center of the continent, reminiscent of the migration of sedimentary depocentres towards the interior of North America (Mitrovica et al., 1989).

However, faster dynamic topography changes can also occur on timescales of one Myr to tens of Myr and can reach up to ± 60 m/Myr in average for both oceans and continents (Fig. 7c). These are linked with abrupt changes in mantle dynamics, such as the initiation, change in the dip angle or break-off of slabs and the rise of a plume head below the lithosphere. We thus expect local stratigraphic sequences with periods ~ 10 Myr to occur in response to mantle flow. These smaller scales of dynamic topography can locally modify shorelines, leading to changes in sedimentation at continental margins as what was observed by Hartley et al. (2011) for the North-European margin in the vicinity of the Iceland plume.

At wavelengths shorter than 500 km, dynamic topography is predominantly controlled by small-scale convection in our models. Petersen et al. (2010) showed that small-scale convection deflects the surface with an amplitude of about $\pm$ 300 m and induces high-frequency (period 2-20 Myr) stratigraphic sequences of about 200 km wavelength. Our whole-mantle convection models suggest that a control of small-scale convection on dynamic topography spatial scales of 200-500 km, of maximal amplitude of ± 750 m and of high-frequency (period 2-50 Myr) is possible and can affect sedimentation and continental flooding at smaller spatial scales. Nevertheless, we observe a partial filtering of small-scale dynamic topography close to continents, which are stiffer and thicker. This rheological attenuation for dynamic mantle tractions by the lithosphere have been studied in laboratory experiments with similar conclusions by Sembroni et al. (2017).

Finally, intermediate to long-wavelength dynamic topography variations caused by changes in the planform of convection due to supercontinent cycles or to the evolution of the number of subduction zones (Fig. 9) are likely to cause changes in the volume of ocean basins (Conrad and Husson, 2009; Spasojevic and Gurnis, 2012), leading to sea-level changes.

5. Conclusion

Our models of whole-mantle convection producing plate-like behaviour successfully produce both small- and large-scale mantle convection. This results in a large diversity of spatial scales of dynamic topography, ranging from very long-wavelength ($>$ 10000 km) to short-wavelength ($<$ 500 km). The spatial scales of predicted dynamic topography are linked to the timing of mantle convective and surface tectonic processes. Subduction initiations, changes in slab-dip angles and slab break-offs modify intermediate wavelengths of several thousands of kilometres on timescales of about one 10-100 Myr. Small-scale dynamic topography ($<$ 500 km) mostly results from the development of small-scale convection below oceanic and continental lithosphere which can lead to short-period variations on the timescale of 1-10 Myr.

This study opens up the prospect of understanding the spatial interplay and the timing of mantle convective processes by studying the past dynamic topography of Earth, not only at large scales but also at shorter wavelengths thanks to the inclusion of a large enough convective vigour and large radial and lateral viscosity contrasts in future 3D models of mantle convection. Previous attempts to reconstruct global present-day residual topography and the past intermediate to long-wavelength residual topography have shown that the hints of dynamic topography-driven features are difficult to isolate and understand, particularly at short wavelengths where lithospheric flexure is important. Nevertheless, our study suggests that the interpretation of surface processes, such as sedimentary series and global sea-level, should include the effect of dynamic topography at all spatial and temporal scales.

6. Acknowledgments

We thank S. Durand for sharing data used in Fig. 3. The research leading to these results has received funding from the European Research Council within the framework of the SP2-Ideas Program ERC-2013-CoG, under ERC grant agreement 617588. Calculations were performed on the Augury supercomputer at P2CHPD Lyon, and with the assistance of resources from the National Computational Infrastructure (NCI), which is supported by the Australian Government. M.A. benefited from funding provided by the grant n°15.007742.01 from Région Rhône-Alpes and a grant from Programme Avenir Lyon Saint-Etienne. N.F. was supported by ARC DE160101020. R.D.M. was supported by ARC IH130200012.

References

Allmann, B.P., Shearer, P.M., 2009. Global variations of stress drop for moderate to large earthquakes. Journal of Geophysical Research: Solid Earth 114. doi:10.1029/2008JB005821.

Amante, C., Eakins, B.W., 2009. ETOPO1 1 arc-minute global relief model: procedures, data sources and analysis. US Department of Commerce, National Oceanic and Atmospheric Administration, National Environmental Satellite, Data, and Information Service, National Geophysical Data Center, Marine Geology and Geophysics Division Colorado. doi:10.1594/PANGAEA.769615.

Brace, W., Kohlstedt, D., 1980. Limits on lithospheric stress imposed by laboratory experiments. Journal of Geophysical Research: Solid Earth 85, 6248–6252. doi:10.1029/JB085iB11p06248.

Butterworth, S., 1930. On the theory of filter amplifiers. Wireless Engineer 7, 536–541.

Chopelas, A., Boehler, R., 1992. Thermal expansivity in the lower mantle. Geophysical Research Letters 19, 1983–1986. doi:10.1029/92GL02144.

Coltice, N., Gérault, M., Ulvrová, M., 2017a. A mantle convection perspective on global tectonics. Earth-Science Reviews 165, 120–150. doi:10.1016/j.earscirev.2016.11.006.

Coltice, N., Larrouturou, G., Debayle, E., Garnero, E.J., 2017b. Interactions of scales of convection in the earth's mantle. Tectonophysics .

Coltice, N., Rolf, T., Tackley, P., Labrosse, S., 2012. Dynamic causes of the relation between area and age of the ocean floor. Science 336, 335–338.

Conrad, C.P., Husson, L., 2009. Influence of dynamic topography on sea level and its rate of change. Lithosphere 1, 110–120. doi:10.1130/L32.1.

Crameri, F., Lithgow-Bertelloni, C., Tackley, P., 2017. The dynamical control of subduction parameters on surface topography. Geochemistry, Geophysics, Geosystems .

Crameri, F., Schmeling, H., Golabek, G., Duretz, T., Orendt, R., Buiter, S., May, D., Kaus, B., Gerya, T., Tackley, P., 2012a. A comparison of numerical surface topography calculations in geodynamic modelling: an evaluation of the 'sticky air' method. Geophysical Journal International 189, 38–54. doi:10.1111/j.1365-246X.2012.05388.x.

Crameri, F., Tackley, P., Meilick, I., Gerya, T., Kaus, B., 2012b. A free plate surface and weak oceanic crust produce single-sided subduction on earth. Geophysical Research Letters 39. doi:10.1029/2011GL050046.

Davaille, A., Le Bars, M., Carbonne, C., 2003. Thermal convection in a heterogeneous mantle. Comptes Rendus Geoscience 335, 141–156. doi:10.1016/S1631-0713(03)00003-8.

Deschamps, F., Tackley, P.J., 2009. Searching for models of thermo-chemical convection that explain probabilistic tomography. ii—influence of physical and compositional parameters. Physics of the Earth and Planetary Interiors 176, 1–18. doi:10.1016/j.pepi.2009.03.012.

Flament, N., Gurnis, M., Müller, R.D., 2013. A review of observations and models of dynamic topography. Lithosphere 5, 189–210. doi:10.1130/L245.1.

Garnero, E.J., McNamara, A.K., Shim, S.H., 2016. Continent-sized anomalous zones with low seismic velocity at the base of earth's mantle. Nature Geoscience doi:10.1038/ngeo2733.

Gillet, P., Daniel, I., Guyot, F., Matas, J., Chervin, J.C., 2000. A thermodynamic model for mgsio 3-perovskite derived from pressure, temperature and volume dependence of the raman mode frequencies. Physics of the Earth and Planetary Interiors 117, 361–384. doi:10.1016/S0031-9201(99)00107-7.

Golle, O., Dumoulin, C., Choblet, G., Cadek, O., 2012. Topography and geoid induced by a convecting mantle beneath an elastic lithosphere. Geophysical Journal International 189, 55–72. doi:10.1111/j.1365-246X.2012.05364.x.

Gurnis, M., 1993. Phanerozoic marine inundation of continents driven by dynamic topography above subducting slabs. Nature 364, 589–593. doi:10.1038/364589a0.

Gvirtzman, Z., Faccenna, C., Becker, T.W., 2016. Isostasy, flexure, and dynamic topography. Tectonophysics 683, 255–271. doi:10.1016/j.tecto.2016.05.041.

Hager, B., Richards, M., 1989. Long-wavelength variations in earth's geoid: physical models and dynamical implications. Philosophical Transactions of the Royal Society of London A: Mathematical, Physical and Engineering Sciences 328, 309–327. doi:10.1098/rsta.1989.0038.

Hansen, U., Yuen, D., Kroening, S., Larsen, T., 1993. Dynamical consequences of depth-dependent thermal expansivity and viscosity on mantle circulations and thermal structure. Physics of the earth and planetary interiors 77, 205–223. doi:10.1016/0031-9201(93)90099-U.

Hartley, R.A., Roberts, G.G., White, N., Richardson, C., 2011. Transient convective uplift of an ancient buried landscape. Nature Geoscience 4, 562–565. doi:10.1038/NGEO1191.

Haxby, W.F., Weissel, J.K., 1986. Evidence for small-scale mantle convection from seasat altimeter data. Journal of Geophysical Research: Solid Earth 91, 3507–3520. doi:10.1029/JB091iB03p03507.

Hernlund, J.W., Tackley, P.J., 2008. Modeling mantle convection in the spherical annulus. Physics of the Earth and Planetary Interiors 171, 48–54. doi:10.1098/rsta.1989.0038.

Hoggard, M., White, N., Al-Attar, D., 2016. Global dynamic topography observations reveal limited influence of large-scale mantle flow. Nature Geoscience doi:10.1038/NGEO2709.

Hoggard, M.J., Winterbourne, J., Czarnota, K., White, N., 2017. Oceanic residual depth measurements, the plate cooling model, and global dynamic topography. Journal of Geophysical Research: Solid Earth 122, 2328–2372. doi:10.1002/2016JB013457.

Husson, L., Guillaume, B., Funiciello, F., Faccenna, C., Royden, L.H., 2012. Unraveling topography around subduction zones from laboratory models. Tectonophysics 526, 5–15. doi:10.1016/j.tecto.2011.09.001.

Jaupart, C., Labrosse, S., Mareschal, J., 2007. 7.06-temperatures, heat and energy in the mantle of the earth. Treatise on geophysics 7, 223–270.

King, S.D., 2009. On topography and geoid from 2-d stagnant lid convection calculations. Geochemistry, Geophysics, Geosystems 10. doi:10.1029/2008GC002250.

Lenardic, A., Moresi, L.N., 1999. Some thoughts on the stability of cratonic lithosphere: Effects of buoyancy and viscosity. Journal of Geophysical Research: Solid Earth 104, 12747–12758. doi:10.1029/1999JB900035.

Lithgow-Bertelloni, C., Silver, P.G., 1998. Dynamic topography, plate driving forces and the african superswell. Nature 395, 269–272. doi:10.1038/26212.

Mitrovica, J., Beaumont, C., Jarvis, G., 1989. Tilting of continental interiors by the dynamical effects of subduction. Tectonics 8, 1079–1094. doi:10.1029/TC008i005p01079.

Molnar, P., England, P.C., Jones, C.H., 2015. Mantle dynamics, isostasy, and the support of high terrain. Journal of Geophysical Research: Solid Earth 120, 1932–1957.

Moresi, L.N., Solomatov, V., 1995. Numerical investigation of 2d convection with extremely large viscosity variations. Physics of Fluids 7, 2154–2162. doi:10.1063/1.868465.

Nakiboglu, S., Lambeck, K., 1980. Deglaciation effects on the rotation of the earth. Geophysical Journal International 62, 49–58. doi:10.1111/j.1365-246X.1980.tb04843.x.

Pekeris, C.L., 1935. Thermal convection in the interior of the earth. Geophysical Journal International 3, 343–367. doi:10.1111/j.1365-246X.1935.tb01742.x.

Petersen, K.D., Nielsen, S., Clausen, O., Stephenson, R., Gerya, T., 2010. Small-scale mantle convection produces stratigraphic sequences in sedimentary basins. Science 329, 827–830. doi:10.1126/science.1190115.

Ricard, Y., 2015. Physics of mantle convection. Treatise of Geophysics , 23–71.

Ricard, Y., Richards, M., Lithgow-Bertelloni, C., Le Stunff, Y., 1993. A geodynamic model of mantle density heterogeneity. Journal of Geophysical Research: Solid Earth 98, 21895–21909. doi:10.1029/93JB02216.

Ritsema, J., Deuss, A., Van Heijst, H., Woodhouse, J., 2011. S40rts: a degree-40 shear-velocity model for the mantle from new rayleigh wave dispersion, teleseismic traveltime and normal-mode splitting function measurements. Geophysical Journal International 184, 1223–1236. doi:10.1111/j.1365-246X.2010.04884.x.

Sembroni, A., Kiraly, A., Faccenna, C., Funiciello, F., Becker, T.W., Globig, J., Fernandez, M., 2017. Impact of the lithosphere on dynamic topography: Insights from analogue modeling. Geophysical Research Letters 44, 2693–2702. doi:10.1002/2017GL072668.

Solomatov, V., Moresi, L.N., 2000. Scaling of time-dependent stagnant lid convection: Application to small-scale convection on earth and other terrestrial planets. Journal of Geophysical Research: Solid Earth 105, 21795–21817.

Spasojevic, S., Gurnis, M., 2012. Sea level and vertical motion of continents from dynamic earth models since the late cretaceous. AAPG bulletin 96, 2037–2064. doi:10.1306/03261211121.

Steinberger, B., 2007. Effects of latent heat release at phase boundaries on flow in the earth's mantle, phase boundary topography and dynamic topography at the earth's surface. Physics of the Earth and Planetary Interiors 164, 2–20. doi:10.1016/j.pepi.2007.04.021.

Tackley, P.J., 2000. Self-consistent generation of tectonic plates in time-dependent, three-dimensional mantle convection simulations. Geochemistry, Geophysics, Geosystems 1. doi:10.1029/2000GC000036.

Tackley, P.J., King, S.D., 2003. Testing the tracer ratio method for modeling active compositional fields in mantle convection simulations. Geochemistry, Geophysics, Geosystems 4. doi:10.1029/2001GC000214.

Tosi, N., Yuen, D.A., de Koker, N., Wentzcovitch, R.M., 2013. Mantle dynamics with pressure-and temperature-dependent thermal expansivity and conductivity. Physics of the Earth and Planetary Interiors 217, 48–58. doi:10.1016/j.pepi.2013.02.004.

Yang, T., Gurnis, M., 2016. Dynamic topography, gravity and the role of lateral viscosity variations from inversion of global mantle flow. Geophysical Journal International 207, 1186–1202. doi:10.1093/gji/ggw335.

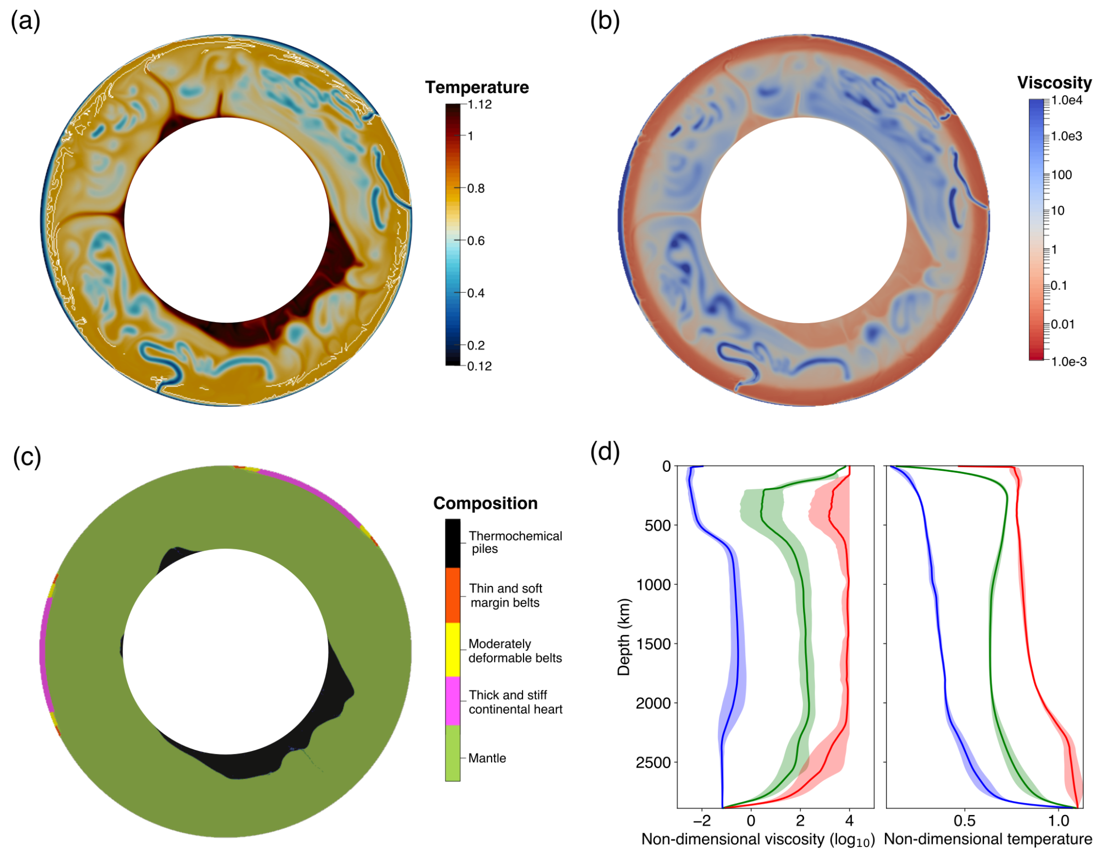

Figure 1: Snapshot of the non-dimensional (a) temperature field with the non-dimensional 0.75 isotherm contoured in white in the upper mantle, (b) viscosity field and (c) composition field for Model 1 with thermo-chemical continental rafts and deep piles. (d) Non-dimensional minimum (blue), mean (green), maximum (red) viscosity and temperature profiles. Envelopes indicate temporal variations in viscosity and temperature. Note the maximum viscosity cutoff at 10^4.

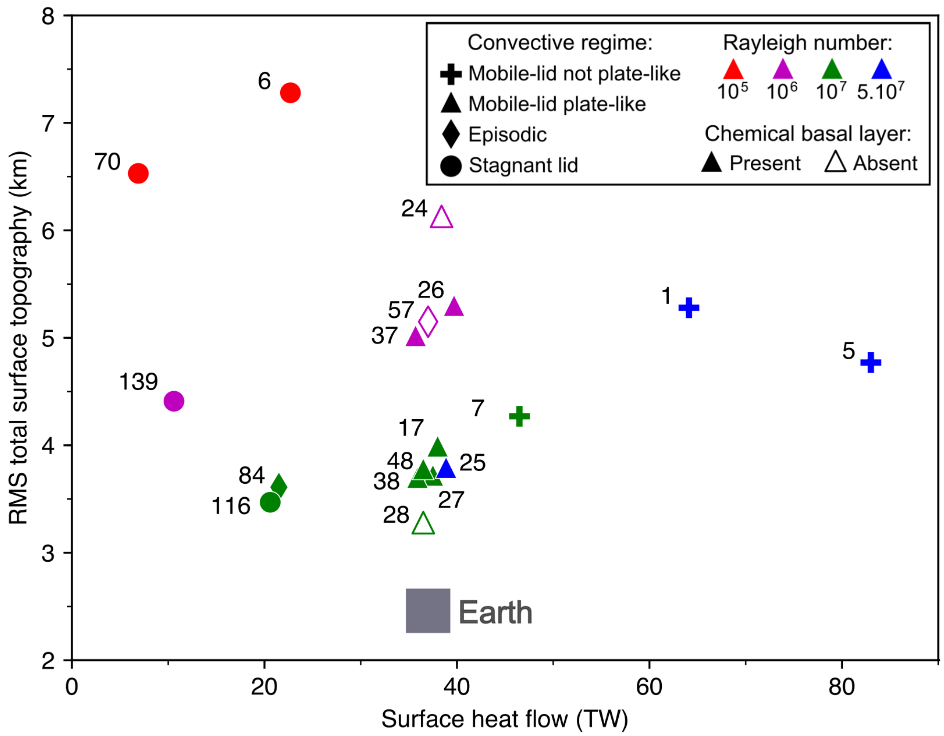

Figure 2: Regime diagram of all our models as a function of the RMS-total surface topography and the surface heat flow. Symbols describe the tectonic regime of our models. Empty and filled symbols represent models respectively excluding and including a chemical basal layer. Colours represent the reference Rayleigh number for each model. The numbers correspond to the dimensional yield-stress of each model in MPa. Earth's surface heat flow corresponds to its total heat flow without the continental crust radioactivity contribution (Jaupart et al., 2007). Earth's surface RMS total topography corresponds to the RMS total topography of Amante and Eakins (2009) after the removal of the loading by oceans.

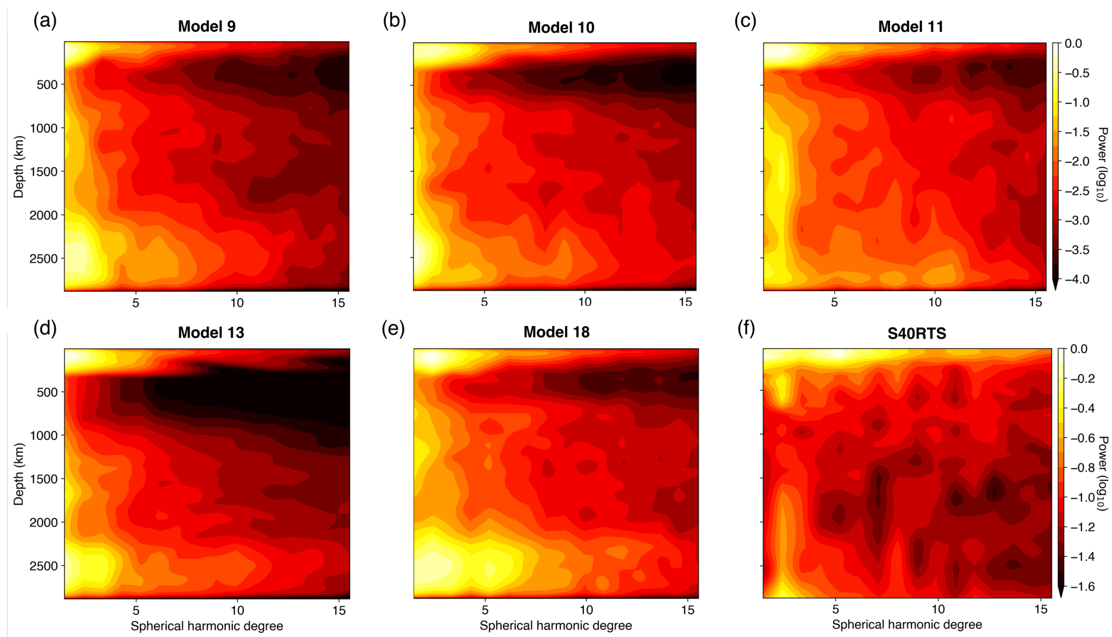

Figure 3: Temporal average of the thermal heterogeneity spectrum for (a) Model 9, (b) Model 10, (c) Model 11, (d) Model 13, and (e) Model 18 normalised by the highest power. (f) is the shear wave velocity heterogeneity spectrum for the S40RTS seismic tomographic model from Ritsema et al. (2011) also normalised by the highest power.

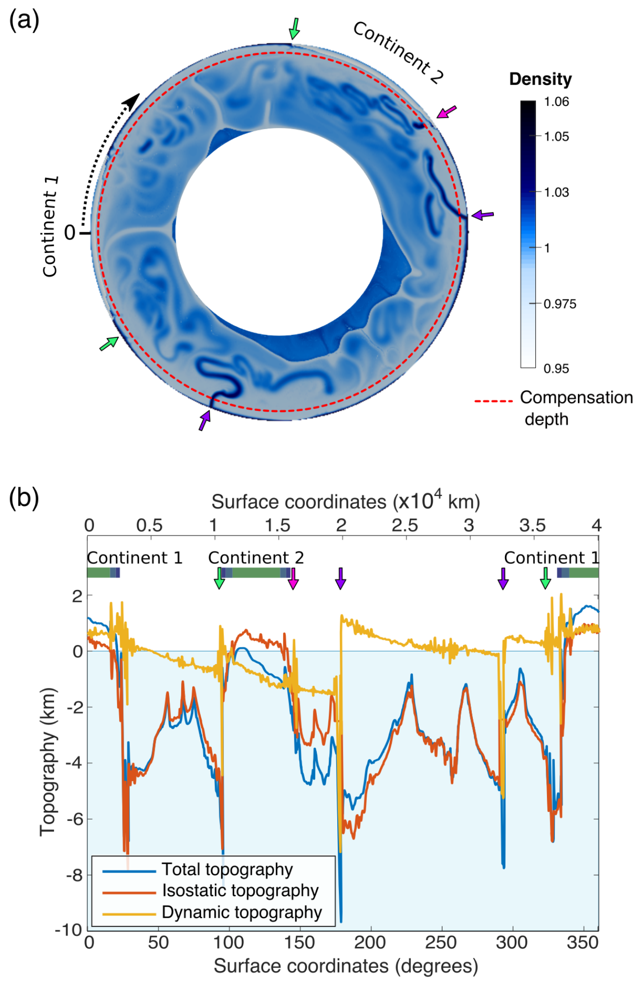

Figure 4: Total topography and its components for Model 10 for the same timestep as Fig. 1. a) Non-dimensional mantle density field. b) Dimensionalised surface total topography (blue) and isostatic (red) and dynamic (yellow) components. Surface coordinates increase clockwise from the left side of the spherical annulus surface, as shown by the black arrow on a). Purple arrows show the locations of ongoing subduction zones, green arrows show the initiation position of future subduction zones and the pink arrow shows a slab break-off event.

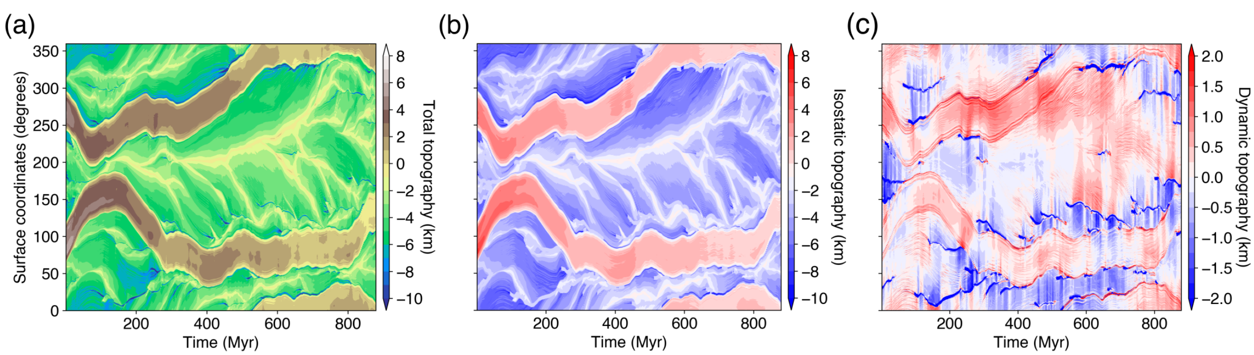

Figure 5: Temporal evolution of (a)total topography, (b) isostatic topography and (c) dynamic topography for Model 10.

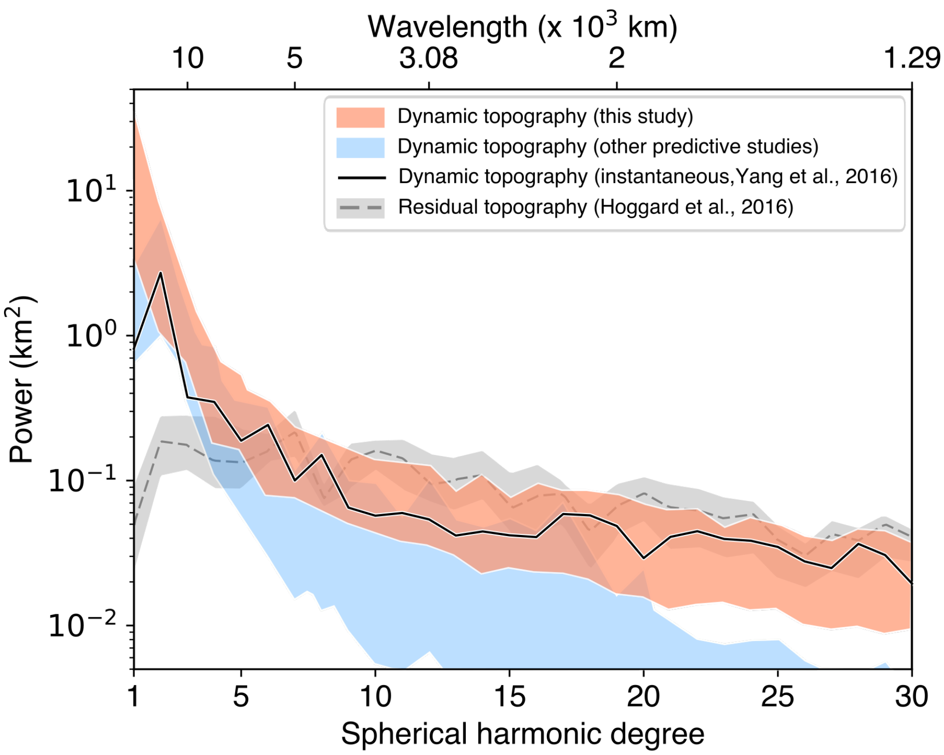

Figure 6: Temporal average of dynamic topography power spectra for our models (orange shaded area). The predictive dynamic topography spectra of Conrad and Husson (2009); Flament et al. (2013); Ricard et al. (1993); Spasojevic and Gurnis (2012); Steinberger (2007) are represented by the light blue envelope. The instantaneous dynamic topography power spectrum of Yang and Gurnis (2016) is represented by the black line. The residual topography power spectrum obtained by regularised least-squares inversion from Hoggard et al. (2016) is shown as a dashed grey line, with the grey envelope representing associated uncertainties.

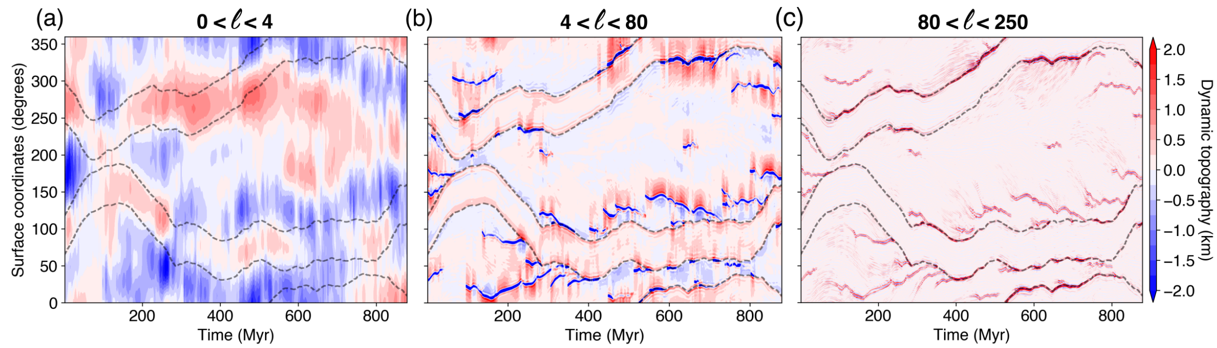

Figure 7: Low-pass, band-pass and high-pass filtered dynamic topography for Model 10. l is the spherical harmonic degree. Continent boundaries are delimitated with dotted grey lines.

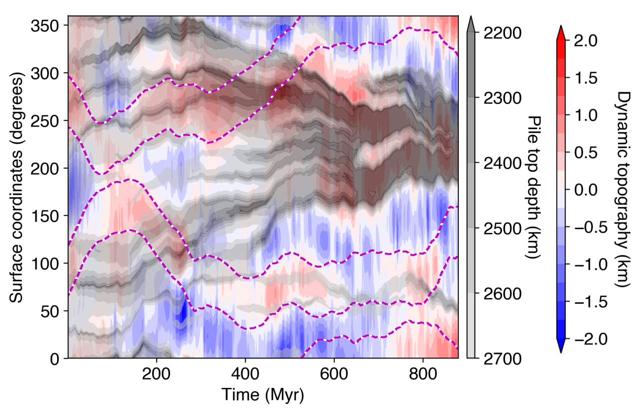

Figure 8: Evolution of the depth of the top of thermo-chemical material. The background blue and red field is the low-pass filtered dynamic topography (Fig. 7a). Magenta dotted lines represent continent boundaries.

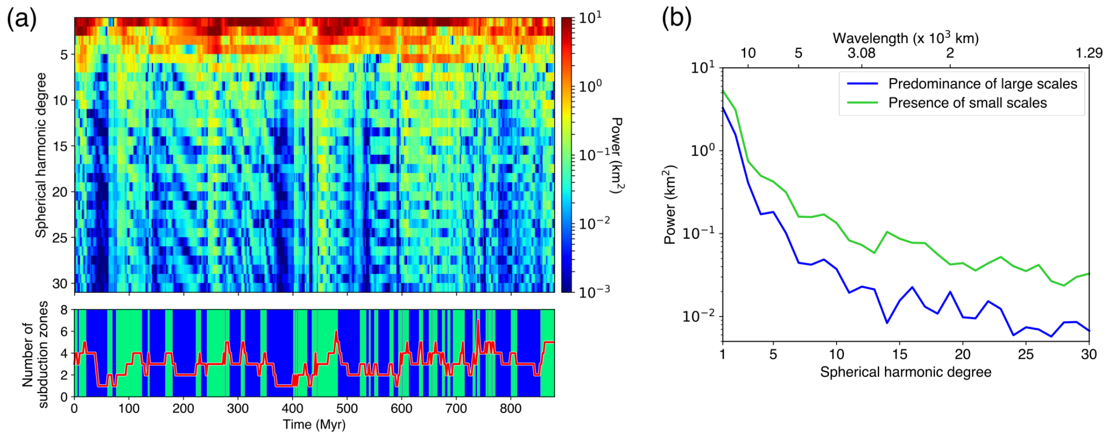

Figure 9: (a) Temporal evolution of dynamic topography power spectrum and evolution of the number of subduction zones through time for Model 10. The blue zones are time intervals where the number of subduction zones decreases or has just decreased. The green regions show the timesteps during which an increase in the number of subduction zones is observed, or directly following an increase of the number of subduction zones. (b) Decomposition of the spectra of dynamic topography for Model 10 according to the separation of spectra for the timesteps following a decrease in the number of subduction zones (blue curve), and those following an increase in the number of subduction zones (green curve). The grey curve, the grey and the blue shaded areas are the same as on Fig. 6.

Table 1: Non-dimensional and dimensional parameters

Parameter	**Non-dim. value**	**Dim. value**
Surface temperature (T_{top})	0.12	255 K
Basal temperature (T_{bot})	1.12	2390 K
Mantle domain thickness (D)	1	2890 km
Reference thermal expansivity (α)	1	5×10^{-5} K^{-1}
Reference density (ρ_0)	1	4400 $kg.m^{-3}$
Reference diffusivity (κ)	1	1×10^{-6} m^2 s^{-1}
Reference conductivity (c_p)	1	3.15 $W.m^{-1}$ K^{-1}
Viscosity constant (A)	-12.5	-88.75
Activation energy (E_a)	8	142 kJ mol^{-1}
Activation volume (V_a)	3	13.8 cm^3 mol^{-1}
Maximum viscosity cutoff	10^4	10^{26} Pa s
Viscosity increase at 660 km	30	
Yield stress gradient for all materials ($d\sigma_Y$)	2.34×10^6	1088 Pa m^{-1}
Yield stress at the surface - continental interior ($\sigma_{Y_{cont}}$)	1×10^6	$312 - 1.2 \times 10^5$ MPa
Viscosity increase - continental interior	1000	
Buoyancy number - continental interior (B_{cont})	-0.41	-225.5 kg m^{-3}
Thickness - continental interior	0.0692	200 km
Yield stress at the surface - continental intermediate belt ($\sigma_{Y_{inter}}$)	4×10^5	$125 - 5.1 \times 10^4$ MPa
Viscosity increase - continental intermediate belt	100	
Buoyancy number - continental intermediate belt (B_{inter})	-0.5	-275 kg m^{-3}
Thickness - continental intermediate belt	0.0432	125 km
Yield stress at the surface - continental margin belt ($\sigma_{Y_{marg}}$)	2×10^5	$62.4 - 2.6 \times 10^4$ MPa
Viscosity increase - continental margin belt	10	
Buoyancy number - continental margin belt (B_{marg})	-0.6	-330 kg m^{-3}
Thickness - continental margin belt	0.0256	75 km
Buoyancy number - deep-seated thermo-chemical layer (B_{llsvp})	0.25	137.5 kg m^{-3}
Initial thickness - deep-seated thermo-chemical layer	0.1038	300 km

Supplementary material for

On the scales of dynamic topography in whole-mantle convection models

Earth and Planetary Science Letters

M. Arnould[a,b,c], N. Coltice[a], N. Flament[c], V. Seigneur[d], R.D. Müller[b]

[a] *CNRS UMR 5276, Université de Lyon, École Normale Supérieure de Lyon, Université Claude Bernard, Laboratoire de Géologie de Lyon, Terre, Planètes, Environnement, 2 rue Raphaël Dubois, Villeurbanne 69622, France*
[b] *EarthByte Group, School of Geosciences, Madsen Building F09, University of Sydney, NSW 2006, Australia*
[c] *School of Earth and Environmental Sciences, University of Wollongong, Northfields Avenue, Wollongong, NSW 2522, Australia*
[d] *CNRS UMR 5669, Université de Lyon, École Normale Supérieure de Lyon, Unité de Mathématiques Pures et Appliquées, 46 Allée d'Italie, 69364 Lyon Cedex 07, France*

SI 1. Comparison of a 1D discrete signal with a 2D signal defined on the sphere $\mathbb{S}^2$

SI 1.1. Notations

We consider a real signal $f : \mathbb{S}^2 \longrightarrow \mathbf{R}$. Its spherical harmonic decomposition can be written:

$$f(\theta, \varphi) = \sum_{l=0}^{\infty} \sum_{m=-l}^{l} f_{l,m} Y_{l,m}(\theta, \varphi),$$

where

$$Y_{l,m}(\theta, \varphi) = \overline{P}_{l,m}(\cos(\theta)) cos(m\varphi)$$

if $m \geq 0$ and

$$Y_{l,m}(\theta, \varphi) = \overline{P}_{l,|m|}(\cos(\theta)) \sin(|m|\varphi)$$

if $m < 0$. We denote by θ the co-latitude, by φ the longitude, and by $\overline{P}_{l,m}$ the Legendre polynomials. We note $g_m(\varphi) = \cos(m\varphi)$ if $m \geq 0$ and $g_m(\varphi) = \sin(|m|\varphi)$ if $m < 0$. We use the fully-normalised Legendre polynomials:

$$\overline{P}_{l,m}(x) = \sqrt{\frac{(2 - \delta_{0,m})(2l + 1)}{4\pi} \frac{(l - m)!}{(l + m)!}} P_{l,m}(x),$$

$$P_{l,m}(x) = (1 - x^2)^{\frac{m}{2}} \frac{d^m}{dx^m} P_l(x),$$

and

$$P_l(x) = \frac{1}{2^l l!} \frac{d^l}{dx^l} (x^2 - 1)^l.$$

$(Y_{l,m})_{l \in \mathbb{N}, m \in \{-l, \ldots, l\}}$ define an orthonormal base for the scalar product $L^2(\mathbb{S}^2, d\Omega)$, with the volume form $d\Omega = |\sin(\theta)| d\theta d\varphi$, where $\theta \in [-\frac{pi}{2}, \frac{pi}{2}]$ and $\varphi \in [0, 2\pi]$.

SI 1.2. Approximation of a function on a sphere by longitudinal functions

The aim here is to show that we can recover a spherical harmonic spectrum from a function defined on a sphere by summing the Fourier spectra of the same function sampled on a large range of great circles.

Let l be an integer, and ϕ_k a group of longitudes respectively equal to $\frac{2\pi k}{N}$, for a large and fixed N. If $f : \mathbb{S}^2 \longrightarrow \mathbf{R}$ is a function defined on the sphere, we can define the function f_l by:

$$f_l(\theta, \varphi) := \sum_{m=-l}^{l} f_{l,m} Y_{l,m}(\theta, \varphi),$$

and for a fixed longitude φ_k, we can define the function f_{l,φ_k} for $\theta \in [-\frac{\pi}{2}, \frac{\pi}{2}]$:

$$f_{l,\varphi_k}(\theta) := f_l(\theta, \varphi_k),$$

and for $\theta \in [-\frac{\pi}{2}, \frac{3\pi}{2}]$:

$$f_{l,\varphi_k}(\theta) := f_l(-\theta + \pi, \pi + \varphi_k)$$

We can extend f_{l,φ_k} to a 2π-periodic function, simply representing the function f_l restricted to the two half-great circles defined by the longitudes φ_k and $\varphi_{k+\frac{N}{2}}$.

We can define, for $j \neq 0$:

$$a_{(l,m),(j,k)} = \frac{1}{\pi} \int_0^{2\pi} Y_{l,m,\varphi_k}(\theta) \sqrt{|\sin(\theta)|} \cos(j\theta) d\theta$$

and

$$b_{(l,m),(j,k)} = \frac{1}{\pi} \int_0^{2\pi} Y_{l,m,\varphi_k}(\theta) \sqrt{|\sin(\theta)|} \sin(j\theta) d\theta,$$

and for $j = 0$:

$$a_{(l,m),(0,k)} = \frac{1}{2\pi} \int_0^{2\pi} Y_{l,m,\varphi_k}(\theta) \sqrt{|\sin(\theta)|} d\theta$$

and

$$b_{(l,m),(0,k)} = 0,$$

the real Fourier coefficients of the θ-dependent function given by $Y_{l,\varphi_k}(\theta)\sqrt{|\sin(\theta)|}$.

The separation of the variables θ and φ in the expression of $Y_{l,m}(\theta, \phi)$ leads to, for any j, k and l:

$$a_{l,(j,k)} = \sum_{m=-l}^{l} g_m(\varphi_k) \frac{2 - \delta_{0,j}}{2\pi} \int_0^{2\pi} \overline{P}_{l,m}(\cos(\theta)) \sqrt{|\sin(\theta)|} \cos(j\theta) d\theta,$$

and to:

$$b_{l,(j,k)} = \sum_{m=-l}^{l} g_m(\varphi_k) \frac{1}{\pi} \int_0^{2\pi} \overline{P}_{l,m}(\cos(\theta)) \sqrt{|\sin(\theta)|} \sin(j\theta) d\theta.$$

Let $\alpha_{j,(l,m)}$ be the Fourier coefficient

$$\alpha_{j,(l,m)} := \frac{2-\delta_{0,j}}{2\pi} \int_0^{2\pi} \overline{P}_{l,m}(\cos(\theta))\sqrt{|\sin(\theta)|}\cos(j\theta)d\theta$$

and $\beta_{j,(l,m)}$ the coefficient:

$$\beta_{j,(l,m)} := \frac{1}{\pi} \int_0^{2\pi} \overline{P}_{l,m}(\cos(\theta))\sqrt{|\sin(\theta)|}\sin(j\theta)d\theta.$$

We want to compare the spherical harmonic power spectrum of f_l given by $S(f_l) = \sum_{m=-l}^{l} f_{l,m}^2$ (with the chosen normalisation conventions), and the k-averaged from 0 to $\frac{N}{2}$ of the Fourier power spectrum of $f_{l,\varphi_k}(\theta)\sqrt{|sin(\theta)|}$.

Therefore, we consider the sum over each k:

$$s_k(f)(\theta) := \sum_{j=0}^{\infty} \sum_{m=-l}^{l} f_{l,m}(a_{j,k}\cos(j\theta) + b_{j,k}\sin(j\theta))$$

for which we want to calculate the spectral power. Its Fourier coefficients are: $\sum_{m=-l}^{l} f_{l,m}a_{j,k}$ and $\sum_{m=-l}^{l} b_{j,k}f_{l,m}$.

Parseval's identity gives:

$$\frac{1}{2\pi}\int_0^{2\pi} s_k(f)(\theta)^2 d\theta = \left(\sum_{m=-l}^{l} f_{l,m}a_{0,k}\right)^2 + \frac{1}{2}\sum_{j=0}^{\infty}\left(\left(\sum_{m=-l}^{l} f_{l,m}a_{j,k}\right)^2 + \left(\sum_{m=-l}^{l} f_{l,m}b_{j,k}\right)^2\right).$$

We name this expression $P_F(s_k(f))$. Let's consider the first sum of the second member of this identity. By taking its square and its average over k, we get:

$$\begin{aligned}
\frac{2}{N}\sum_{k=0}^{\frac{N}{2}-1}\sum_{m=-l}^{l}\sum_{m'=-l}^{l} f_{l,m}f_{l,m'}a_{0,k}^2 &= \sum_{m=-l}^{l}\sum_{m'=-l}^{l} f_{l,m}f_{l,m'}\frac{2}{N}\sum_{k=0}^{\frac{N}{2}-1} a_{0,k}^2 \\
&= \sum_{m=-l}^{l}\sum_{m'=-l}^{l} f_{l,m}f_{l,m'}\alpha_{0,(l,m)}\alpha_{0,(l,m')}\frac{2}{N}\sum_{k=0}^{\frac{N}{2}-1} g_m(\varphi_k)g_{m'}(\varphi_k)
\end{aligned}$$

This last equation contains a Riemann sum for each m, for which the convergence rate only depends on m and thus on l. We therefore have:

$$\frac{2}{N}\sum_{k=0}^{\frac{N}{2}-1} g_m(\varphi_k)g_{m'}(\varphi_k) = \frac{2}{N}\sum_{k=0}^{\frac{N}{2}-1} g_m(\pi k\frac{2}{N})g_{m'}(\pi k\frac{2}{N}),$$

For a large N, this gives:

$$\frac{2}{N}\sum_{k=0}^{\frac{N}{2}-1} g_m(\varphi_k)g_{m'}(\varphi_k) \approx \int_0^1 g_m(\pi t)g_{m'}(\pi t)dt$$

(we can replace the '$\approx$' sign by an '$=$' sign if N tends to infinity.) After a simple calculation, this gives:

$$\frac{2}{N}\sum_{k=0}^{\frac{N}{2}-1} g_m(\varphi_k)g_{m'}(\varphi_k) \approx \delta_{m,m'}\int_0^1 g_m(\pi t)^2 dt$$

We recall that $g_m(\pi t)^2$ is equal to $\cos(m\pi t)^2$ for any positive m and to $\sin(m\pi t)^2$ for any negative m. We therefore have, for any $m \neq 0$:

$$\int_0^1 g_m(\pi t)^2 dt = \frac{1}{2}$$

and

$$\int_0^1 g_0(\pi t)^2 dt = 1.$$

The sum over m and m' then leads to:

$$\sum_{m=-l}^{l}\sum_{m'=-l}^{l} f_{l,m}f_{l,m'}\alpha_{0,(l,m)}\alpha_{0,(l,m')}\frac{2}{N}\sum_{k=0}^{\frac{N}{2}-1} g_m(\varphi_k)g_{m'}(\varphi_k) \approx \sum_{m=0}^{l}\alpha_{0,(l,m)}^2\frac{1}{2}(f_{l,m}^2+f_{l,-m}^2).$$

The approximation is valid because the rate of convergence only depends on l.

We can do the same calculations for any j. We then get, for any $j \geq 1$:

$$\frac{2}{N}\sum_{k=0}^{\frac{N}{2}-1}\left(\sum_{m=-l}^{l} f_{l,m}a_{j,k}\right)^2 \approx \sum_{m=0}^{l}\alpha_{j,(l,m)}^2\frac{1}{2}(f_{l,m}^2+f_{l,-m}^2)$$

and

$$\frac{2}{N}\sum_{k=0}^{\frac{N}{2}-1}\left(\sum_{m=-l}^{l} f_{l,m}b_{j,k}\right)^2 \approx \sum_{m=0}^{l}\beta_{j,(l,m)}^2\frac{1}{2}(f_{l,m}^2+f_{l,-m}^2).$$

Finally, this leads to:

$$\frac{2}{N}\sum_{k=0}^{\frac{N}{2}-1}P_F(s_k(f)) \approx$$

$$\sum_{m=0}^{l}\alpha_{0,(l,m)}^2\frac{1}{2}(f_{l,m}^2+f_{l,-m}^2)+\frac{1}{2}\sum_{j=1}^{\infty}\left(\sum_{m=0}^{l}\alpha_{j,(l,m)}^2\frac{1}{2}(f_{l,m}^2+f_{l,-m}^2)+\sum_{m=0}^{l}\beta_{j,(l,m)}^2\frac{1}{2}(f_{l,m}^2+f_{l,-m}^2)\right).$$

By inverting the two sums, we have:

$$\frac{2}{N}\sum_{k=0}^{\frac{N}{2}-1}P_F(s_k(f)) \approx \sum_{m=0}^{l}\frac{1}{2}(f_{l,m}^2+f_{l,-m}^2)\left(\alpha_{0,(l,m)}^2+\frac{1}{2}\sum_{j=1}^{\infty}\alpha_{j,(l,m)}^2+\beta_{j,(l,m)}^2\right).$$

The sum over j contains the Fourier development of $\overline{P}_{l,m}(\cos(\theta)\sqrt{|\sin(\theta)|}$.
Thanks to the Parseval's identity, we know that this sum equals to:

$$\frac{1}{2\pi}\int_{-\pi}^{\pi}\overline{P}_{l,m}(\cos(\theta))^2|\sin(\theta)|d\theta.$$

The change of variables $u = \cos(\theta)$ leads to:

$$\frac{1}{\pi}\int_{-1}^{1}\overline{P}_{l,m}(u)^2du$$

which is equal to $\frac{2(2-\delta_{0,m})}{4\pi^2}$.

Finally, we get, by dividing the sum with the part of negative m:

$$\frac{2}{N}\sum_{k=0}^{\frac{N}{2}-1}P_F(s_k(f)) \approx \frac{1}{2\pi^2}\sum_{m=-l}^{l}f_{l,m}^2.$$

Therefore,

$$\frac{2}{N}\sum_{k=0}^{\frac{N}{2}-1}\int_0^{2\pi} s_k(f)(\theta)^2 d\theta \approx \frac{1}{\pi}\times S(f_l).$$

In conclusion, in order to retrieve the spherical harmonic power of a 2D signal f_l defined on the sphere $\mathbb{S}^2$ from Fourier power spectra of the same signal f_{l,φ_k} restricted to two half great-circles defined by the longitudes φ_k and $\varphi_{k+\frac{N}{2}}$, we need to consider the sum over a large range N of longitudes of the Fourier spectral power coefficients of the following function $f_{l,\varphi_k}\sqrt{|sin(\theta)|}$, then divided by π.

We applied this method to the dynamic topography field of Flament et al. (2013). We decomposed this field into 180 signals defined on longitudinal great circles. We then calculated their corresponding Fourier spectra accordingly to the method described before. We averaged the resulting power spectral coefficients of all great circles for each frequence k and compared the resulting spectrum with the known spherical harmonic spectrum of the whole field (Fig. SI 1).

From Fig. SI 1, we show that we successfully recover the spherical harmonic power spectrum of Flament et al. (2013) by using the method described before. The two curves are not exactly superposed because we only averaged Fourier spectra over 180 great circles. However, the method described before is exact for an infinite number of signals restricted to longitudinal great circles.

We repeated the same process for different dynamic topography global fields (Ricard et al., 1993; Steinberger, 2007; Conrad and Husson, 2009; Spasojevic and Gurnis, 2012; Yang and Gurnis, 2016), and the residual topography field of Hoggard et al. (2016), with same positive conclusions.

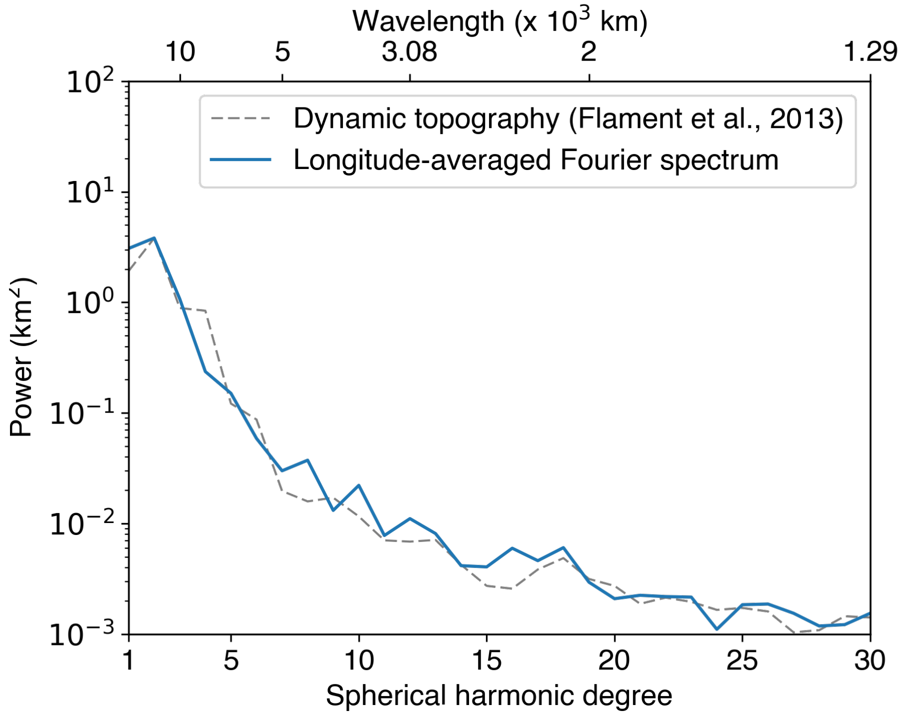

Figure SI 1: Comparison of the spherical harmonic spectrum of dynamic topography from Flament et al. (2013) with the longitudinal average of the Fourier power spectra of dynamic topography by Flament et al. (2013), sampled over 180 longitudinal great circles.

When we calculate dynamic topography power spectra for our models, we repeat the procedure described above and add a correction of the slope of the Fourier power spectra by dividing the amplitude of each spherical harmonic degree l by $2l + 1$ to account for the degree-dependent slope of spherical harmonics decomposition (Maus, 2001).

SI 2. Parameters used in this study and applicability to Earth's surface and mantle dynamics

Table SI 1: Model input parameters and resulting output. Ra is the Rayleigh number, H the internal heat production rate, CBL means Chemical Basal Layer, $\sigma_{Y_{oc}}$ is the surface oceanic lithosphere yield stress, P the plateness, M the mobility, Q_0 the surface heat flow, h_{RMS} the surface total RMS topography, q_0/q_{CMB} the ratio of CMB to surface heat flux, T_{LAB} the sub-lithospheric temperature, and η_0 the reference viscosity.

	Input parameters				Surface characteristics				Mantle properties		
Model	**Ra**	**H ($\mathbf{W.kg^{-1}}$)**	$\boldsymbol{\sigma_{\mathbf{Y_{oc}}}}$ **(MPa)**	**CBL**	**P**	**M**	$\mathbf{Q_0}$ **(TW)**	$\mathbf{h_{RMS}}$ **(km)**	$\mathbf{q_0/q_{CMB}}$	$\mathbf{T_{LAB}}$	$\boldsymbol{\eta_0}$ **(Pa s)**
Model 1	10^5	8.7×10^{-13}	6.37	Yes	0.13	0.16	22.7	7.28	6 %	0.78	1.1×10^{24}
Model 2	10^5	1.9×10^{-12}	70	Yes	0.94	0.97	6.9	6.53	19 %	0.72	1.2×10^{24}
Model 3	10^6	3.8×10^{-12}	139	Yes	0.88	0.47	10.6	4.41	25 %	0.72	1.2×10^{23}
Model 4	10^6	9.1×10^{-12}	26.2	Yes	0.86	1.01	39.7	5.30	7 %	0.76	1.1×10^{23}
Model 5	10^6	8.5×10^{-12}	24.8	No	0.91	1.13	38.4	6.13	7 %	0.80	1.0×10^{23}
Model 6	10^6	8.5×10^{-12}	37.1	Yes	0.93	0.93	35.7	5.02	8 %	0.80	1.0×10^{23}
Model 7	10^6	7.8×10^{-12}	57	No	0.97	0.86	37	5.15	8 %	0.86	9.5×10^{22}
Model 8	10^7	1.2×10^{-11}	7.42	Yes	0.88	1.15	46.4	4.27	8 %	0.68	1.2×10^{22}
Model 9	10^7	9.7×10^{-12}	16.9	Yes	0.93	0.97	38	3.98	10 %	0.74	1.2×10^{22}
Model 10	10^7	9.2×10^{-12}	27	Yes	0.97	0.85	37.5	3.72	9 %	0.75	1.1×10^{22}
Model 11	10^7	9.7×10^{-12}	28	No	0.95	1.03	36.5	3.28	15 %	0.71	1.2×10^{22}
Model 12	10^7	8.8×10^{-12}	38.2	Yes	0.97	0.88	35.9	3.70	8 %	0.78	1.1×10^{22}
Model 13	10^7	8.4×10^{-12}	48.8	Yes	0.96	0.80	36.5	3.78	9%	0.81	1.0×10^{22}
Model 14	10^7	8.2×10^{-12}	84.3	Yes	0.92	0.60	21.5	3.61	20 %	0.82	1.0×10^{22}
Model 15	10^7	7.8×10^{-12}	116	Yes	-0.1	0.00	20.6	3.47	7 %	0.85	9.7×10^{21}
Model 16	5×10^7	9.2×10^{-12}	5.3	Yes	0.87	1.25	83	4.77	10 %	0.75	2.2×10^{21}
Model 17	5×10^7	1.4×10^{-11}	1.25	Yes	0.91	1.08	64.1	5.28	13 %	0.65	2.6×10^{21}
Model 18	5×10^7	9.7×10^{-12}	25	Yes	0.97	0.82	38.9	3.79	13 %	0.65	2.6×10^{21}
Earth	$\mathbf{10^{7.5}\text{-}10^9}$	**3-5** $\mathbf{\times 10^{-12}}$[a]	**10-500**[b]	??	$>$ **0.75**[c]	??	**37-41**[d]	**2.460**[e]	?? %	**0.64**[f]	??

[a] Present-day heat production rate deduced from the activity of radioactive elements K,U and Th (Turcotte and Schubert, 2014)

[b] Stress release from earthquakes (Allmann and Shearer, 2009) and high-pressure high-temperature experiments (Brace and Kohlstedt, 1980)

[c] Earth's lowest bound plateness taken from f_{90} estimated by Kreemer et al. (2014)(at least 14%).

[d] Earth's total surface heat flow without continental lithosphere radioactive heat production (Jaupart et al., 2007).

[e] RMS-total topography of Earth from etopo1 (Amante and Eakins, 2009) after the removal of the loading of oceans.

[f] Non dim. sub-lithospheric temperature assuming the isotherm 1600 K.

We calculated the temporal average of the hypsometric distribution for Models 9, 10, 11, 13 and 18 (Fig. SI 2) to further characterise the total topography of our models.

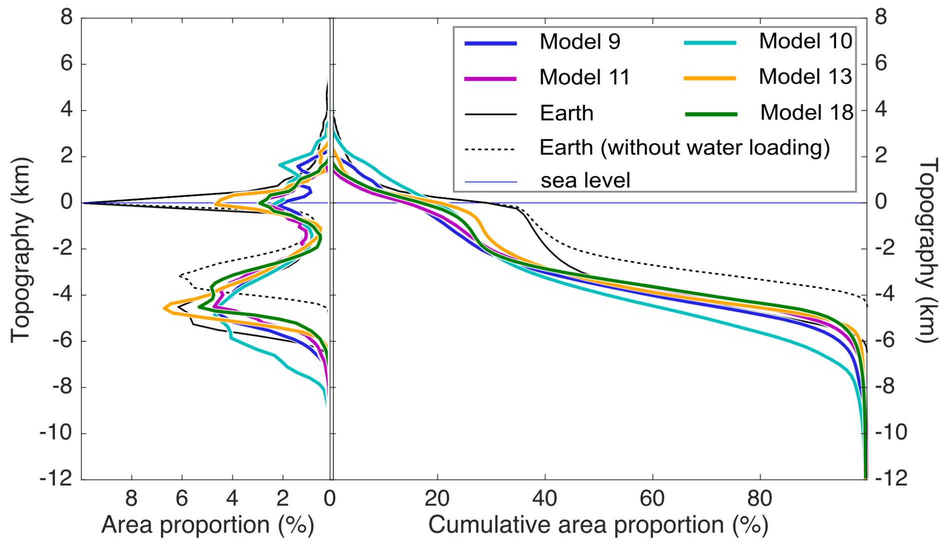

Figure SI 2: Hypsometry for Models 9, 10, 11, 13 and 18 (time averaged, resp. blue, cyan, magenta, orange and green) and Earth (etopo1 (Amante and Eakins, 2009), black solid line). The black dotted line is Earth's hypsometry unloaded for ocean water assuming isostasy.

SI 3. Temporal evolution of the surface total, isostatic and dynamic topography in different models generating plate-like tectonics

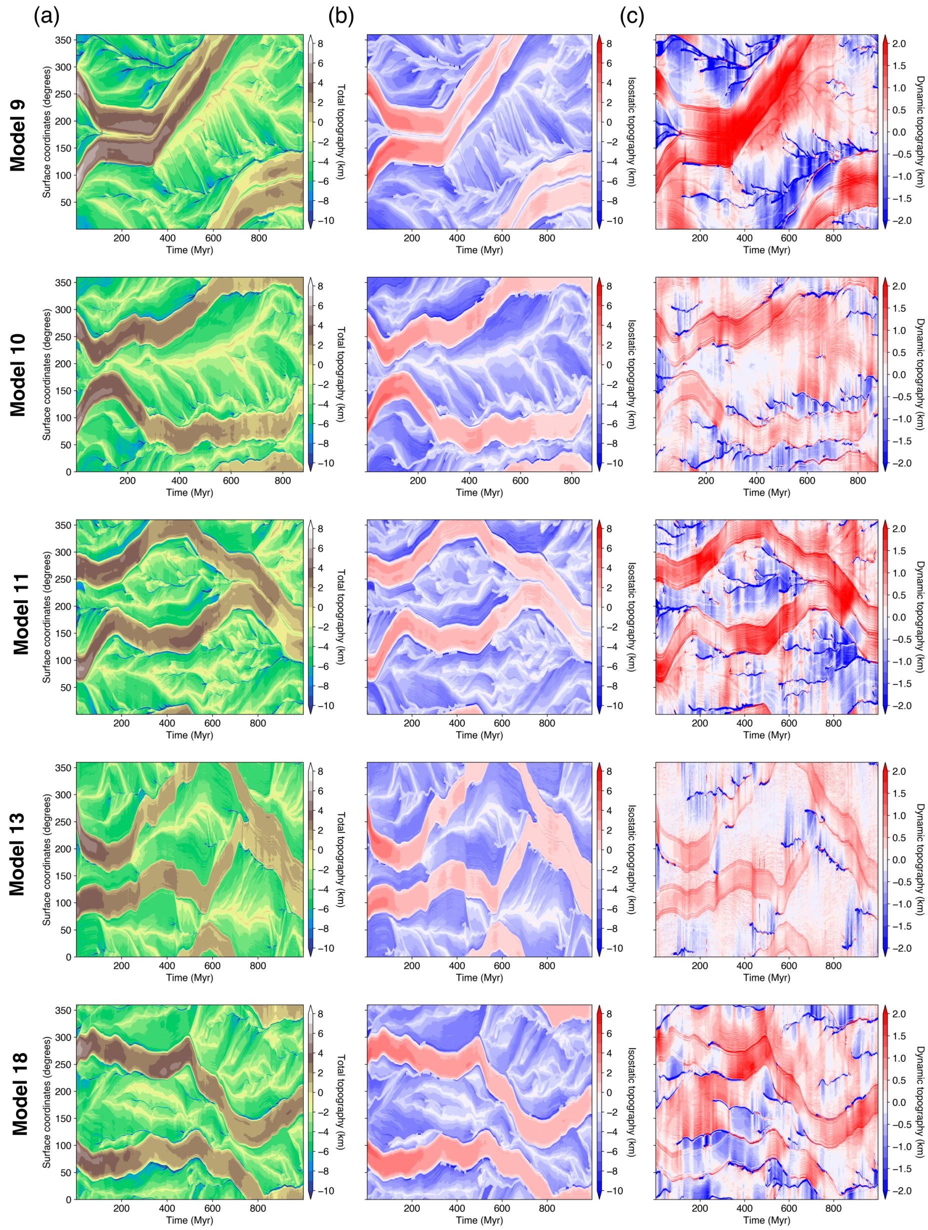

Figure SI 3: Temporal evolution of (a) total topography, (b) isostatic topography and (c) dynamic topography for Models 9, 10, 11, 13 and 18.

SI 4. Variation of the assumed lateral extent of subduction zones

To calculate dynamic topography, we assume that the topography at subduction zones is entirely dynamic. We arbitrarily set the lateral extent of subduction zones to 500 km in our study. We verified that increasing or decreasing this value does not significantly affect the spatial distribution of dynamic topography (Fig. SI 4).

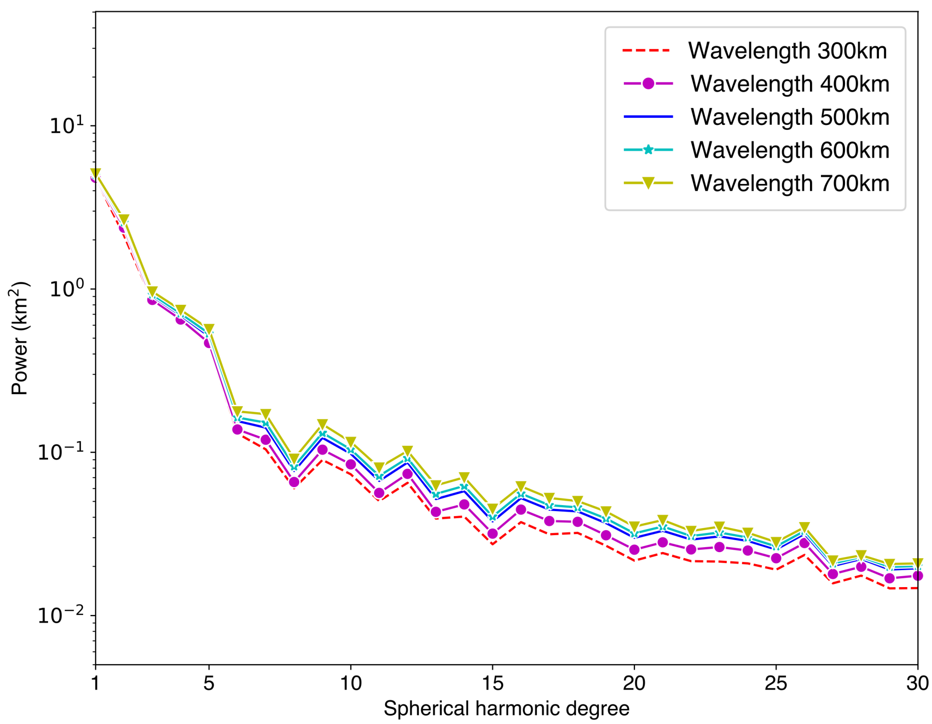

Figure SI 4: Influence of the lateral width (wavelength) of subduction zones on the resulting spectrum of dynamic topography for Model 10.

References

Allmann, B.P., Shearer, P.M., 2009. Global variations of stress drop for moderate to large earthquakes. Journal of Geophysical Research: Solid Earth 114. doi:10.1029/2008JB005821.

Amante, C., Eakins, B.W., 2009. ETOPO1 1 arc-minute global relief model: procedures, data sources and analysis. US Department of Commerce, National Oceanic and Atmospheric Administration, National Environmental Satellite, Data, and Information Service, National Geophysical Data Center, Marine Geology and Geophysics Division Colorado. doi:10.1594/PANGAEA.769615.

Brace, W., Kohlstedt, D., 1980. Limits on lithospheric stress imposed by laboratory experiments. Journal of Geophysical Research: Solid Earth 85, 6248–6252. doi:10.1029/JB085iB11p06248.

Conrad, C.P., Husson, L., 2009. Influence of dynamic topography on sea level and its rate of change. Lithosphere 1, 110–120. doi:10.1130/L32.1.

Flament, N., Gurnis, M., Müller, R.D., 2013. A review of observations and models of dynamic topography. Lithosphere 5, 189–210. doi:10.1130/L245.1.

Hoggard, M., White, N., Al-Attar, D., 2016. Global dynamic topography observations reveal limited influence of large-scale mantle flow. Nature Geoscience doi:10.1038/NGEO2709.

Jaupart, C., Labrosse, S., Mareschal, J., 2007. 7.06-temperatures, heat and energy in the mantle of the earth. Treatise on geophysics 7, 223–270.

Kreemer, C., Blewitt, G., Klein, E.C., 2014. A geodetic plate motion and global strain rate model. Geochemistry, Geophysics, Geosystems 15, 3849–3889.

Maus, S., 2001. New statistical methods in gravity and magnetics.

Ricard, Y., Richards, M., Lithgow-Bertelloni, C., Le Stunff, Y., 1993. A geodynamic model of mantle density heterogeneity. Journal of Geophysical Research: Solid Earth 98, 21895–21909. doi:10.1029/93JB02216.

Spasojevic, S., Gurnis, M., 2012. Sea level and vertical motion of continents from dynamic earth models since the late cretaceous. AAPG bulletin 96, 2037–2064. doi:10.1306/03261211121.

Steinberger, B., 2007. Effects of latent heat release at phase boundaries on flow in the earth's mantle, phase boundary topography and dynamic topography at the earth's surface. Physics of the Earth and Planetary Interiors 164, 2–20. doi:10.1016/j.pepi.2007.04.021.

Turcotte, D., Schubert, G., 2014. Geodynamics. Cambridge University Press.

Yang, T., Gurnis, M., 2016. Dynamic topography, gravity and the role of lateral viscosity variations from inversion of global mantle flow. Geophysical Journal International 207, 1186–1202. doi:10.1093/gji/ggw335.